

Large-eddy simulations of a lean hydrogen premixed turbulent jet flame with tabulated chemistry

Emiliano M. Fortes^a, Eduardo J. Pérez-Sánchez^a, Temistocle Grenga^b,
Michael Gauding^c, Heinz Pitsch^c, Daniel Mira^{a,*}

^aBarcelona Supercomputing Center (BSC), Plaça Eusebi Güell, 1-3 08034, Barcelona, Spain

^bFaculty of Engineering and Physical Sciences, University of Southampton, SO17 1BJ, Southampton, United Kingdom

^cInstitute for Combustion Technology, RWTH Aachen University, 52056 Aachen, Germany

Abstract

Large-eddy simulations (LES) of a planar turbulent lean hydrogen–air jet flame at $Re = 11000$ are performed using a tabulated flamelet model based on mixture-averaged diffusion that incorporates detailed transport, including differential and preferential diffusion, wall heat loss, and thermodiffusion. The approach is extended to turbulent combustion in LES using a presumed-shape probability density function formulation that accounts for sub-filter effects. The flame exhibits a highly corrugated front, driven by local variations of mixture fraction induced by strong thermodiffusive transport. These effects significantly alter both the flame structure and morphology. The LES results are systematically compared to a reference direct numerical simulation across varying LES filters through different mesh resolutions to evaluate the predictive capability of the model. The LES accurately reproduces instantaneous flow structures and thermodiffusive effects. Global flame characteristics including flame length, surface area, and consumption speed, are well captured and show limited sensitivity to mesh resolution. The role of thermodiffusion is also examined, showing that its incorporation leads to a more reactive flame and should not be neglected in the formulation. Heat losses are incorporated into the tabulated chemistry framework for completeness but are found to have a negligible impact, consistent with the walls weak influence in the present configuration. Overall, the results demonstrate that the proposed approach provides reliable predictions of the main flame characteristics, with remaining discrepancies primarily associated with unresolved sub-filter effects that deserve further investigation.

Keywords: Tabulated chemistry, Preferential diffusion, Differential diffusion, Hydrogen, Turbulent Jet Flame, Large Eddy Simulation, LES, Direct Numerical Simulation, DNS

* Barcelona Supercomputing Center (BSC), Plaça Eusebi Güell, 1-3 08034, Barcelona, Spain

Novelty and significance statement

This work introduces a significant advance in the predictive modelling of lean hydrogen turbulent flames by formulating a tabulated chemistry framework that captures the full complexity of mixture-averaged transport, preferential and differential diffusion, wall heat loss, and thermodiffusion in the context of LES. Unlike prior studies that rely on simplified transport closures or constant Lewis numbers, the present approach embeds detailed molecular and thermal diffusion physics while retaining computational efficiency. Its significance lies in demonstrating that such a comprehensive treatment of transport phenomena enables accurate representation of thermodiffusive behaviour and flame topology in turbulent hydrogen combustion. This establishes a more physically grounded basis for modelling low-Lewis-number flames and strengthens the reliability of flamelet-based LES for hydrogen combustion.

e-mail: daniel.mira@bsc.es (Daniel Mira)

1. Introduction

Hydrogen has emerged as a leading candidate towards net-zero CO₂ emissions due to its strong potential to drive sustainable energy solutions. However, several challenges are associated with the use of this fuel, including high flame speed, high mass diffusivity, low volumetric energy density, NO_x emissions, and enhanced instabilities, all of which add complexity to the deployment of hydrogen for industrial applications [1]. Burning hydrogen under lean conditions offers a practical mitigation strategy, as it moderates some of these adverse effects, particularly NO_x formation. However, this benefit comes at the cost of enhanced thermodiffusive effects, whose accurate representation remains a modelling challenge for Large-Eddy Simulations (LES) [2].

In hydrogen flames, differential and preferential transport play an important role within the flame structure. Preferential diffusion arises from the disparity between mass and thermal diffusivities, leading in lean hydrogen–air mixtures to a very low fuel Lewis number ($Le_{H_2} \approx 0.3 \ll 1$). Preferential diffusion results from unequal species diffusivities, such that Le_i varies among species. While present in all fuels, these effects are particularly pronounced in lean hydrogen flames, where they strongly influence the burning velocity and promote thermodiffusive instabilities [3, 4, 5]. Detailed analyses identify differential diffusion as the primary mechanism driving flame corrugation [1] and, consequently, exerting a dominant influence on global flame characteristics. Differential diffusion contributes to local enrichment in flame regions of positive curvature or fuel depletion in negative curvature regions (seen from fresh gases), further promoting the formation of thermodiffusive instabilities [1]. In addition, the Soret effect further enhances these instabilities, although its contribution is comparatively weaker [6, 7, 8].

Tabulated chemistry (TC) methods offer a powerful strategy for simulating turbulent combustion, providing a practical route to incorporate complex transport and chemical phenomena while maintaining computational efficiency [9]. Accordingly, a range of modelling strategies has been developed to account for these thermodiffusive effects within TC frameworks. Early approaches focused on determining effective Lewis numbers from 1D laminar structures [10] and on introducing additional transport terms and modulated flux coefficients into the governing equations for the controlling variables [11, 12, 13, 14]. This methodology has been successfully applied to stratified hydrogen flames, blends, and LES configurations [15, 16, 17]. Alternative formulations have sought to improve accuracy by reformulating the transport terms. Regele et al. [18] and Schlup et al. [19] introduced source terms to account for differential diffusion and the Soret effect within the mixture fraction equation. Other strategies involve transporting species mass fractions to reconstruct the manifold coordinates [20, 21] or using commuting operators under constant Lewis number assumptions to derive new transport coefficients [22]. While these models have demonstrated excellent predictive capabilities in laminar flame configurations, their application to turbulent flames subjected to strong thermodiffusive effects is less common. Nicolai et al. [14] applied a high-dimensional tabulation strategy to explicitly account for differential diffusion in stratified hydrogen–methane flames using LES and quantified its impact with experimental data. Almutairi et al. [17] used a TC model including preferential diffusion for Reynolds-Averaged Navier-Stokes simulations of hydrogen-enriched flames on a dual-fuel engine, showing improved agreement with experiments in terms of pressure traces and heat-release rates compared with diffusion-neutral tabulations.

More recently, several studies have focused specifically on lean hydrogen flames with thermodiffusive insta-

bilities. Berger et al. [23] applied an LES combustion model incorporating the extended version of Regele's model [18] for thermodiffusive transport by Schlup and Blanquart [8, 19] into a filtered progress variable/mixture fraction description, and performed *a priori* and *a posteriori* assessments using Direct Numerical Simulations (DNS) data [24]. Ferrante et al. [25] investigated different closures for differential diffusion, including the models of Regele et al. [18] and Mukundakumar et al. [22] for partially premixed hydrogen flames in the framework of presumed filtered probability density function for LES. Masucci et al. [26] assessed the capabilities of LES combined with flamelet models for both premixed and non-premixed hydrogen flames, highlighting the potential of tabulated approaches for low-emission gas-turbine applications, but also pointing out limitations related to preferential diffusion and near-wall phenomena.

Despite these advances, validations of tabulated chemistry models against DNS for turbulent hydrogen flames subject to strong thermodiffusive instabilities remain limited. The objective of the present work is to address this gap through a comprehensive assessment of a TC framework based on mixture-averaged diffusion developed in previous studies by the authors [27], which has recently been validated in several studies [4, 28, 29], but extended to LES using a presumed-shape PDF approach [16, 30]. Particular attention is given to evaluating the sensitivity of the predictions to mesh resolution and to the treatment of complex transport phenomena. To this end, LES results are benchmarked against the high-fidelity DNS data of a planar turbulent premixed hydrogen–air jet flame investigated by Berger et al. [24]. In addition to the grid-resolution study, a set of simulations are defined to isolate the effects of wall heat loss and thermodiffusion, enabling a quantitative assessment of their relative impact on flame topology, consumption speed, flame length, and overall model accuracy.

The paper is organised as follows. Section 2 introduces the tabulated-chemistry formulation, including its extension to LES. Section 3 details the numerical framework, including the transport equations for LES, sub-filter models, and the construction of the laminar flame manifolds. Section 4 describes the planar turbulent premixed jet configuration, the reference DNS, and the set of LES cases with the different physics comprised. The results are presented in Section 5, where a dedicated analysis is conducted to assess the predictive capabilities of the different modelling features across different mesh resolutions. Finally, conclusions and perspectives for future work are summarised in Section 6.

2. Model description

The modelling of hydrogen flames requires the accurate prediction of diffusive fluxes across the flame front to account for preferential and differential diffusion. To capture these effects, species diffusion is modelled using a mixture-averaged diffusion formulation, which accounts for the effect of the mixture molecular weight and a velocity correction for mass conservation [31, 27]. Additionally, thermal diffusion, also known as the Soret effect, is included due to its significance when the flame is curved [19].

For a mixture of N_s species the mixture-averaged diffusion model with the Soret effect approximates the mass diffusion fluxes for each species $k = 1, \dots, N_s$ as:

$$\mathbf{V}_k Y_k = -\frac{W_k}{W} D_k \nabla X_k - \frac{D_k^T}{\rho T} \nabla T, \quad (1)$$

where \mathbf{V}_k is the diffusion velocity of the k -th species (vectors are denoted in bold characters), X_k and Y_k are its

molar and mass fractions, respectively, $D_k = 1 - Y_k / \sum_{j=1, j \neq k}^{N_s} X_j / \mathcal{D}_{jk}$ is the diffusion coefficient, W_k and W denote the molecular weights of the species and the mixture, respectively, \mathcal{D}_{jk} are the binary diffusion coefficients of the j -th into the k -th species, T denotes the temperature and D_k^T is the thermal diffusion coefficient of the k -th species.

Rewriting the species flux in terms of the mass fraction and including the velocity correction \mathbf{V}_c (such that $\sum_{j=1}^{N_s} (\mathbf{V}_k + \mathbf{V}_c) Y_k = 0$), the mass diffusive flux for the k -th species takes the form:

$$\begin{aligned} \mathbf{j}_k = & -\frac{W_k}{W} D_k \nabla X_k + Y_k \sum_{j=1}^{N_s} \frac{W_j}{W} D_j \nabla X_j \\ & - \frac{D_k^T}{\rho T} \nabla T + Y_k \sum_{j=1}^{N_s} \frac{D_j^T}{\rho T} \nabla T. \end{aligned} \quad (2)$$

In TC methods, the manifold representing all possible thermochemical states Ψ of the flames is parametrised by a set of N_c controlling variables $(\mathcal{Y}_1, \dots, \mathcal{Y}_{N_c})$, such that $\Psi = \Psi(\mathcal{Y}_1, \dots, \mathcal{Y}_{N_c})$. Therefore, the physical gradient of the dependent variables can be expressed through the chain rule in terms of the gradients of the controlling variables and the gradients of the manifold's dependent variables in phase space. Accordingly, the gradient operator in the TC framework can be rewritten as $\nabla = \sum_{i=1}^{N_c} \nabla \mathcal{Y}_i \frac{\partial}{\partial \mathcal{Y}_i}$, and the species fluxes can be written in the compact form $\mathbf{j}_k = -\sum_{i=1}^{N_c} \Lambda_{Y_k, \mathcal{Y}_i} \nabla \mathcal{Y}_i$, where:

$$\begin{aligned} \Lambda_{Y_k, \mathcal{Y}_i} = & \frac{W_k}{W} D_k \frac{\partial X_k}{\partial \mathcal{Y}_i} - Y_k \sum_{j=1}^{N_s} D_j \frac{W_j}{W} \frac{\partial X_j}{\partial \mathcal{Y}_i} \\ & + \frac{D_k^T}{\rho T} \frac{\partial T}{\partial \mathcal{Y}_i} - Y_k \sum_{j=1}^{N_s} \frac{D_j^T}{\rho T} \frac{\partial T}{\partial \mathcal{Y}_i}. \end{aligned} \quad (3)$$

The coefficients $\Lambda_{Y_k, \mathcal{Y}_i}$ depend only on the flame structure in phase space and, therefore, can be expressed as a function of $(\mathcal{Y}_1, \dots, \mathcal{Y}_{N_c})$ and stored in look-up tables [27].

If the fluxes of the control variables are defined as functions of the fluxes of the manifold-dependent variables, transport equations for the controlling variables can be derived. In particular, if they are defined as linear combinations of species mass fractions, the controlling variables transport equations can be derived by linearly combining the species transport equations, which are given by:

$$\rho \frac{\partial Y_k}{\partial t} + \rho \mathbf{u} \cdot \nabla Y_k + \nabla \cdot (\rho \mathbf{j}_k) = \dot{\omega}_k. \quad (4)$$

By applying the equality of Eq. (3) to Eq. (4), the controlling variables transport equations take the following general form:

$$\rho \frac{\partial \mathcal{Y}_i}{\partial t} + \rho \mathbf{u} \cdot \nabla \mathcal{Y}_i = \sum_{j=1}^{N_c} \nabla \cdot (\rho \Gamma_{\mathcal{Y}_i, \mathcal{Y}_j} \nabla \mathcal{Y}_j) + \dot{\omega}_{\mathcal{Y}_i}, \quad (5)$$

where coefficients $\Gamma_{\mathcal{Y}_i, \mathcal{Y}_j}$ are the result of linearly combining coefficients $\Lambda_{Y_k, \mathcal{Y}_i}$ according to the definition of the controlling variables, and $\dot{\omega}_{\mathcal{Y}_i}$ denotes their associated source terms. Using this notation, the diffusive flux for the controlling variables can be expressed as $\mathbf{j}_{\mathcal{Y}_i} = \sum_{j=1}^{N_c} (\Gamma_{\mathcal{Y}_i, \mathcal{Y}_j} \nabla \mathcal{Y}_j)$.

For the particular configuration studied in this work, wall heat losses are included in the injection [24], and therefore, for completeness, the TC method must also account for these effects. For manifolds with heat losses,

the typical choice for the controlling variables includes a reactive progress variable Y_c , the mixture fraction Z and the total enthalpy h . For the h equation, the dissipation term due to viscous forces is neglected. Then, the resulting transport equation has the same structure as Eq. (5) with no source term and a diffusive flux defined by Fourier's law, and given by:

$$\mathbf{j}_h = - \sum_{i=1}^{N_c} \left(\frac{\lambda}{\rho} \frac{\partial T}{\partial \mathcal{Y}_i} + \sum_{k=1}^{N_s} \Lambda_{Y_k, \mathcal{Y}_i} h_k \right) \nabla \mathcal{Y}_i = - \sum_{i=1}^{N_c} \Gamma_{h, \mathcal{Y}_i} \nabla \mathcal{Y}_i, \quad (6)$$

where λ is the thermal conductivity and h_k is the specific enthalpy for the k -th species [27].

In practice, it is convenient to use normalised control variables for tabulation. Therefore, the space of (Y_c, Z, h) is transformed into the manifold of (c, Z, I) variables for the cases with heat loss, where c and I are the normalised progress variable and normalised enthalpy, respectively, defined as:

$$c(Y_c, Z) = \frac{Y_c - Y_{c,u}(Z)}{Y_{c,b}(Z) - Y_{c,u}(Z)}, \quad (7)$$

$$I(c, Z, h) = \frac{h - h_{\min}(c, Z)}{h_{\max}(c, Z) - h_{\min}(c, Z)}. \quad (8)$$

While the formulation described above provides a complete description of the flame structure in phase space, its application to turbulent combustion requires a statistical treatment of the governing equations. In the LES framework, the large-scale features of the flow are resolved, while the effects of smaller sub-filter scales must be modelled. To this end, the laminar transport equations are subjected to a Favre-filtering operation, introducing sub-filter terms that account for turbulent transport and the interaction between turbulence and chemistry at the sub-filter scale.

To obtain the transport equations for the Favre-filtered controlling variables, we follow the same procedure commonly adopted in previous tabulated-chemistry formulations for turbulent combustion [15, 16, 17]. Applying Favre filtering to the governing equations given by Eq. (5) yields the LES filtered transport equations for \tilde{Y}_c , \tilde{Z} , and \tilde{h} :

$$\begin{aligned} \frac{\partial(\bar{\rho} \tilde{Y}_c)}{\partial t} + \nabla \cdot (\bar{\rho} \tilde{\mathbf{u}} \tilde{Y}_c) = \bar{\omega}_{Y_c} \\ + \nabla \cdot \left(\bar{\rho} \left[\tilde{\Gamma}_{Y_c, Y_c} + \frac{v_t}{Sc_t} \right] \nabla \tilde{Y}_c + \bar{\rho} \tilde{\Gamma}_{Y_c, Z} \nabla \tilde{Z} \right) \end{aligned} \quad (9)$$

$$\begin{aligned} \frac{\partial(\bar{\rho} \tilde{Z})}{\partial t} + \nabla \cdot (\bar{\rho} \tilde{\mathbf{u}} \tilde{Z}) = \\ \nabla \cdot \left(\bar{\rho} \left[\tilde{\Gamma}_{Z, Z} + \frac{v_t}{Sc_t} \right] \nabla \tilde{Z} + \bar{\rho} \tilde{\Gamma}_{Z, c} \nabla \tilde{c} \right) \end{aligned} \quad (10)$$

$$\begin{aligned} \frac{\partial(\bar{\rho} \tilde{h})}{\partial t} + \nabla \cdot (\bar{\rho} \tilde{\mathbf{u}} \tilde{h}) = \\ \nabla \cdot \left(\bar{\rho} \left[\tilde{\Gamma}_{h, h} + \frac{v_t}{Sc_t} \right] \nabla \tilde{h} + \bar{\rho} \tilde{\Gamma}_{h, c} \nabla \tilde{c} \right) \end{aligned} \quad (11)$$

where a gradient flux hypothesis has been applied to model the sub-filter fluxes and Sc_t denotes the turbulent Schmidt number. Additional governing equations can be obtained for higher moments, such as the Favre sub-filter variances of progress variable variance $Y_{c,v} := \widetilde{Y_c^2} - \widetilde{Y_c}^2$ and mixture fraction variance $Z_v := \widetilde{Z^2} - \widetilde{Z}^2$. The transport equations for $Y_{c,v}$ and Z_v are given as follows:

$$\begin{aligned} \frac{\partial(\bar{\rho} Y_{c,v})}{\partial t} + \nabla \cdot (\bar{\rho} \tilde{\mathbf{u}} Y_{c,v}) = \nabla \cdot \left(\bar{\rho} \left[\tilde{\Gamma}_{Y_c, Y_c} + \frac{\nu_t}{Sc_t} \right] \nabla Y_{c,v} \right) \\ + 2\bar{\rho} \frac{\nu_t}{Sc_t} \nabla \tilde{Y}_c \cdot \nabla \tilde{Y}_c \\ - \bar{\rho} C_{Y_c} \frac{\nu_t}{Sc_t} \frac{Y_{c,v}}{\Delta^2} + 2(\overline{Y_c \dot{\omega}_{Y_c}} - \tilde{Y}_c \overline{\dot{\omega}_{Y_c}}), \end{aligned} \quad (12)$$

$$\begin{aligned} \frac{\partial(\bar{\rho} Z_v)}{\partial t} + \nabla \cdot (\bar{\rho} \tilde{\mathbf{u}} Z_v) = \nabla \cdot \left(\bar{\rho} \left[\tilde{\Gamma}_{Z,Z} + \frac{\nu_t}{Sc_t} \right] \nabla Z_v \right) \\ + 2\bar{\rho} \frac{\nu_t}{Sc_t} \nabla \tilde{Z} \cdot \nabla \tilde{Z} - \bar{\rho} C_Z \frac{\nu_t}{Sc_t} \frac{Z_v}{\Delta^2}, \end{aligned} \quad (13)$$

where scalar dissipation rate of the variances is modulated with constants C_{Y_c} and C_Z . Enthalpy variances are not considered.

The coefficients in these equations are obtained by integrating the manifold according to a presumed joint-Probability Density Function (jPDF) in (c, Z, I) , where I is a normalised enthalpy [30]. Since no sub-filter variance is considered for the enthalpy, the distribution in I is represented by a Dirac delta centred at the filtered value \tilde{I} , so that the filtered vector for the thermochemical state is given by:

$$\tilde{\Psi} = \int_0^1 \int_0^1 \Psi(c, Z, \tilde{I}) P(c, Z; \tilde{c}, c_v, \tilde{Z}, Z_v) dc dZ. \quad (14)$$

Under the additional assumption of statistical independence between c and Z , the jPDF factorises as:

$$P(c, Z; \tilde{c}, c_v, \tilde{Z}, Z_v) = P_c(c; \tilde{c}, c_v) P_Z(Z; \tilde{Z}, Z_v), \quad (15)$$

where \tilde{c} and c_v denote the filtered mean and sub-filter variance of the normalised progress variable. In this work, beta PDFs are used to model both P_c and P_Z . A recent study by Berger et al. [2] examined this dependence in detail and proposed strategies to account for it. Assessing the validity of the statistical independence assumption is left for future work.

3. Numerical framework

The DNS simulation corresponds to that of Berger et al. [24], to which the reader is referred for numerical details, and is used here for the assessment of the LES solutions. A skeletal mechanism with nine species and nineteen reactions for hydrogen–air combustion, proposed by Burke et al. [32], is employed in both the DNS and LES simulations. For the DNS, constant Lewis numbers obtained in the burnt mixture from one-dimensional flame calculations are imposed [24], whereas for the LES, molecular diffusivity is modelled using the mixture-averaged diffusion formulation. Note that the codes use different numerical methods, which could influence the direct comparison between solutions. One-dimensional flame results confirm that constant Lewis numbers and mixture-averaged transport yield nearly identical global flame parameters across the range of equivalence ratios

encountered in the jet simulation (see supplementary material). Consequently, the choice of diffusion model should have a negligible influence on the 3D results, a conclusion further supported by the simulation results presented in this work.

For the LES, the governing equations for continuity, momentum, enthalpy, controlling variables, and associated sub-filter variances given by Eqs.(9)-(13) are solved under the low-Mach-number assumption, with the mixture treated as an ideal gas. Sub-filter fluxes are modelled using the gradient flux hypothesis, and the Vreman model [33] is applied to define the sub-grid eddy viscosity, with a model constant of $C_k = 0.1$. In these simulations, the turbulent Schmidt number is set to $Sc_t = 0.7$, while constants C_{Y_c} and C_Z for the dissipation of the variances of the progress variable and mixture fraction are set as in previous studies [30, 34]. The full set of equations is solved using the code Alya [35], which employs a low-dissipation, single-stage numerical scheme for velocity-pressure coupling [34]. The scalar transport equations for the turbulent controlling variables are solved with a second-order spatial discretisation scheme based on the Algebraic Subgrid Scale (ASGS) method and using linear finite elements [36]. All governing equations are advanced in time using an explicit third-order Runge-Kutta scheme [34].

Combustion model

Laminar flame manifolds are generated by solving unstretched, adiabatic one-dimensional premixed flames with the Cantera solver V3.0 [37], using the mixture-averaged diffusion model. The Soret effect is included following the Chapman–Cowling formulation for mixture-averaged transport [38, 39], a treatment that has recently been assessed in the context of hydrogen flames [8, 40].

The manifolds are constructed in two stages. First, a set of adiabatic, isobaric, premixed one-dimensional hydrogen–air flames is computed for an unburnt-gas temperature of $T_u = 298\text{K}$. Next, flamelets at lower enthalpy levels are obtained using a burner-stabilised configuration [41], with the burner temperature fixed at the wall temperature, $T_{\text{wall}} = 298\text{K}$. A sequence of such flamelets is then computed by prescribing the inlet mass flux as a fraction of the mass flux of the corresponding adiabatic flame at T_u , progressively reducing it to achieve increasing levels of heat loss to the burner.

Water vapour is used as the progress variable, $Y_c = Y_{\text{H}_2\text{O}}$. For \tilde{Y}_c , the discretisation consists of 101 linearly spaced points from 0 to 1 in normalised progress variable space. For the filtered mixture fraction and enthalpy, the discretisations include 58 and 17 points, respectively. The scaled variance variables are discretised with 11 points following a cubic law.

4. Case configuration

The case corresponds to a planar turbulent premixed jet flame with a main injection of hydrogen–air mixture at an equivalence ratio of 0.4 at atmospheric pressure and ambient temperature. The main injection is surrounded by a hot co-flow with a composition corresponding to the burnt gases at equilibrium considering the main jet composition (therefore, the mixture fraction values for both the inlet and the co-flow are equal). The mixture exhibits an effective Lewis number $Le_{\text{eff}} \approx 0.346$ (estimated as in [42]), which is below its critical Lewis number $Le_c \approx 0.824$ (calculated according to Sivashinsky’s theory for weak thermal expansion [43]). The Karlovitz number based on the unstretched 1D flame speed and thickness is relatively low in this case (estimated at $Ka \approx 15$ [24]),

which amplifies thermodiffusive effects and supports the applicability of scale-separation-based approaches such as flamelet models. Under these conditions, the combined influence of species diffusion and thermal diffusion introduces a destabilising effect on the flame. As demonstrated by Berger et al. [24] through comparisons between DNS flames with $Le \neq 1$ and $Le = 1$, thermodiffusive effects have a leading order effect on the flame dynamics.

A three-dimensional computational domain is employed, consisting of a main hydrogen–air injection channel of length $H = 8$ mm aligned with the y -direction and bounded by solid walls of finite thickness w_t in the x -direction. The channel ends in a rectangular volume, which serves as the computational domain in this study, with only a section of height H from the injection channel as part of the domain. The remainder of the cross-stream extent is supplied by the hot co-flow, and the domain is periodic in the spanwise (z) direction. The main injection has a bulk velocity of 24 m s^{-1} , while the co-flow is injected at 3.6 m s^{-1} . Given that the separation between the plates is $H = 8$ mm, the jet Reynolds number for the main injection is $Re = 11000$.

The DNS reference case uses a structured hexahedral mesh with a total number of elements of $(N_x, N_y, N_z) = (1472, 1792, 512)$ and constant spacing $\delta_{x,z}^{\text{DNS}} = 70 \mu\text{m}$. Turbulent inlet conditions are mapped directly from an auxiliary channel simulation. No-slip and isothermal $T_{\text{wall}} = 298 \text{ K}$ boundary conditions are applied at the walls. The wall thickness is set to $w_t = 3\delta_{x,z}^{\text{DNS}} = 0.21 \text{ mm}$.

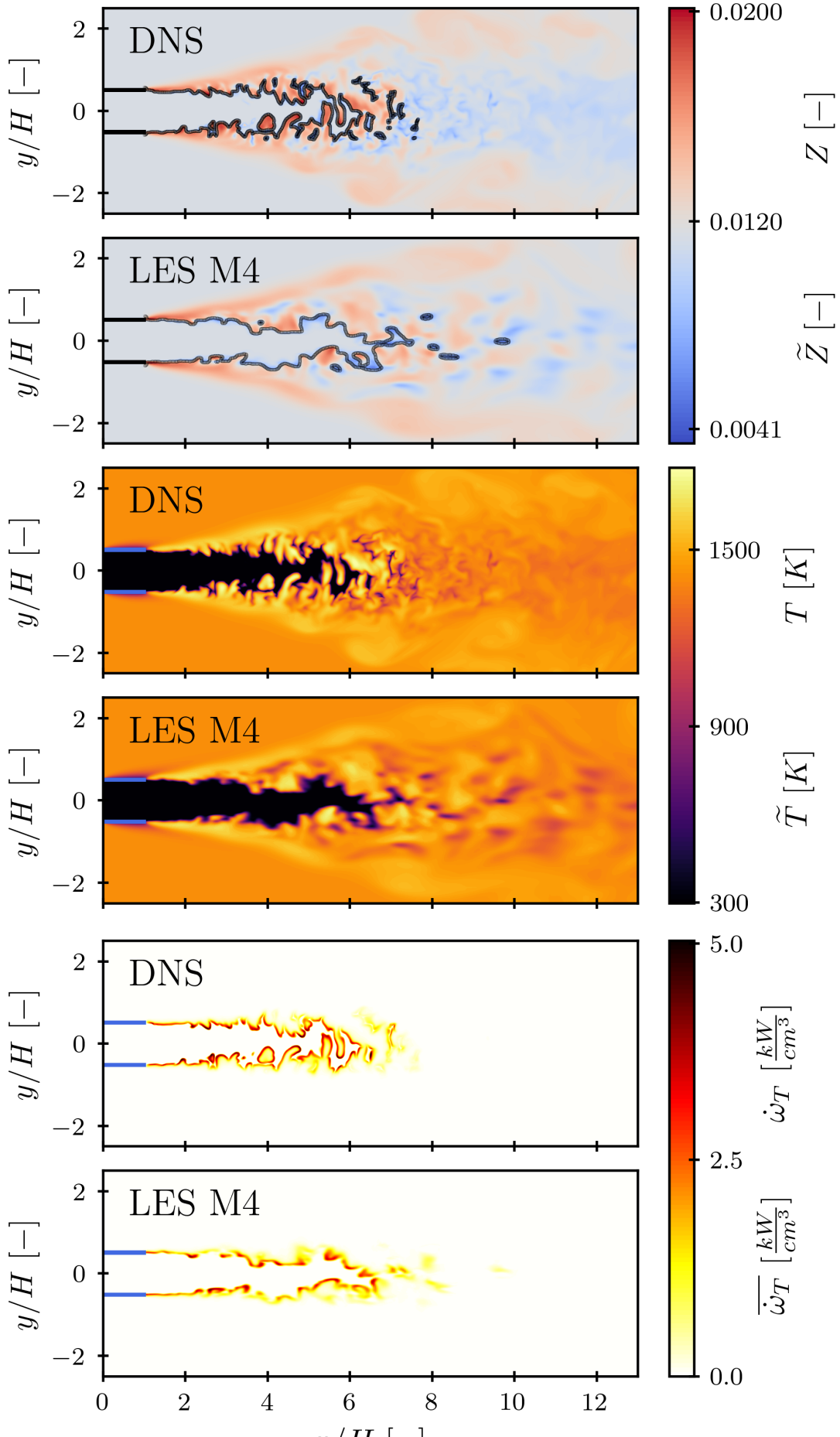
The LES also uses a structured mesh composed of hexahedra, but the mesh is coarsened towards the outlet in the x -direction and the lateral sides in the y -direction, so that the aspect ratio of the elements is kept constant in the diagonal, using geometrical expansion with ratios of 1.037 and 1.005 in the crosswise and streamwise directions, respectively. Four meshes (M1–M4) evaluate resolution effects by scaling element sizes relative to the wall thickness (w_t). Note that the present study uses implicit filtering, which means that each mesh resolution also features different LES filter size. From M1 to M4, inlet and spanwise resolutions are 0.5, 1, 1.5, and 2 points per w_t , respectively. Wall resolution is 1 point per w_t for M1–M2 and 2 points for M3–M4. This refinement increases the total element count from 2 M (M1) to 9.5 M (M2), 23 M (M3), and 42 M (M4). The meshes have a maximum resolution at the injection of 6, 3, 2 and 1.5 times δ_{DNS} and coarsen up to approximately 9.4, 6.5, 5.6 and 5 times $\delta_{x,z}^{\text{DNS}}$ at the average flame tip. Additional details of the meshes are provided in the supplementary material.

Turbulent inlet conditions for each LES are provided by a set of precursor channel flow simulations with streamwise (x) and spanwise (z) periodicity at the corresponding LES resolution. The conditions are set for the same bulk Reynolds number using a wall model [44]. Fully developed spatial solutions are mapped to the jet inlet. Jet flame simulations apply a wall model to the channel walls and slip conditions to lateral boundaries.

The simulations considered in this study are given in Table 1. One simulation including heat loss ($T_{\text{wall}} = 298 \text{ K}$) and Soret is performed for each mesh (M1 to M4), while two additional simulations using mesh M4 were also conducted to evaluate independently the effects of heat loss and thermodiffusion, ‘LES M4 no D_k^T ’ and ‘LES M4 no T_{wall} ’, respectively. The objective of these additional simulations is to provide complementary insights into the overall influence of different physical processes within tabulated-chemistry approaches.

5. Results and discussion

This section provides a systematic comparison between the DNS reference solutions and six LES cases that employ different mesh resolutions and closures for thermodiffusive transport, and heat loss effects. The analysis is



Case	T_{wall}	D_k^T	CV
LES M4	298 K	ON	$(\widetilde{Z}, \widetilde{Y}_c, \widetilde{h}, \widetilde{Z}_v, Y_{c,v})$
LES M4 no D_k^T	298 K	OFF	$(\widetilde{Z}, \widetilde{Y}_c, \widetilde{h}, \widetilde{Z}_v, Y_{c,v})$
LES M4 no T_{wall}	Adiabatic	ON	$(\widetilde{Z}, \widetilde{Y}_c, \widetilde{Z}_v, Y_{c,v})$
LES M3	298 K	ON	$(\widetilde{Z}, \widetilde{Y}_c, \widetilde{h}, \widetilde{Z}_v, Y_{c,v})$
LES M2	298 K	ON	$(\widetilde{Z}, \widetilde{Y}_c, \widetilde{h}, \widetilde{Z}_v, Y_{c,v})$
LES M1	298 K	ON	$(\widetilde{Z}, \widetilde{Y}_c, \widetilde{h}, \widetilde{Z}_v, Y_{c,v})$

Table 1: Table of LES simulations. The column CV stands for controlling variables. The mesh refines from M1 to M4.

performed to assess the ability of the proposed tabulated flamelet model to reproduce the fundamental characteristics of turbulent premixed hydrogen flames and its sensitivity to the mesh resolution (M1 to M4).

5.1. Instantaneous fields

In lean hydrogen flames, the low Lewis number promotes thermodiffusive instabilities that result in highly corrugated flame fronts. The combined action of this corrugation and turbulence increases the global consumption speed and flame surface area, while locally modifying the flame structure and reactivity ratio [24, 45]. A key aspect of LES is the modelling of chemical source terms and transport properties required to predict the flame structure and dynamics. This becomes particularly relevant when thermodiffusive effects dominate, as unresolved sub-filter contributions may have some influence that is difficult to infer from the resolved scales. Consequently, assessing the impact of mesh resolution with their associated changes in filter size is essential to evaluate the accuracy and predictability of the proposed LES. In this section, a quantitative analysis based on the instantaneous fields is presented, with particular emphasis on the role of spatial resolution.

The instantaneous fields of mixture fraction Z , temperature T , and heat release rate $\dot{\omega}_T$ from the DNS along with the corresponding Favre-filtered LES quantities for the finest mesh (M4), are shown in Fig. 1. The visualisations illustrate the impact of thermodiffusive effects on flame morphology. To highlight the flame shape, the level curve corresponding to a scaled temperature $T_s = 0.6$ is added on the subplots, where:

$$T_s = \frac{T - T_u}{T_b^{1D} - T_u}, \quad (16)$$

and $T_b^{1D} = 1421.95$ K denotes the equilibrium temperature of the adiabatic one-dimensional flame at the inlet equivalence ratio. For the LES case, the same definition is retained, but the instantaneous T is replaced by instantaneous \widetilde{T} .

Two distinct regions are observed in physical space. The first corresponds to the primary reaction zone, characterised by an envelope of high heat release where alternating concave and convex fronts are present, forming finger-like structures, a characteristic feature of turbulence with thermodiffusive instabilities. In regions where the flame front is concave (relative to the fresh gases), thermodiffusive effects reduce the local mixture fraction, lowering temperatures and attenuating heat release. Conversely, convex regions exhibit local enrichment of the mixture, leading to super-adiabatic temperatures and intensified reaction rates. Further downstream of the primary reaction zone, pockets of both enriched and depleted mixture fraction emerge. However, depleted regions are predominant, leading to a heterogeneous, layered flow structure characterised by alternating zones of high and relatively

low temperature. The second region consists of two lateral branches that exhibit significant local enrichment and super-adiabatic temperatures, but with negligible heat release. As illustrated in Fig. 1, these complex phenomena are successfully captured by the present turbulent combustion model.

The influence of grid resolution on the first region is detailed in Fig. 2. In the LES, due to the inherent resolution limits of the LES meshes and the use of low-order (second-order) numerical schemes, a significant portion of the fine-scale flame wrinkling remains unresolved and partially dissipated. Since local variability in the mixture fraction is largely driven by flame curvature arising from both complex flame dynamics and thermodiffusive effects, this unresolved wrinkling directly results in attenuated fluctuations. Consequently, the LES mixture fraction field appears more uniform than the DNS. Furthermore, while the current model captures curvature-driven behaviour at resolved scales [4], it lacks an explicit sub-filter formulation to recover the curvature fluctuations below the filter-size. As a result, the correlation between the scalar fields in LES and DNS improves substantially as the mesh is refined from M1 to M4.

The instantaneous results show that the proposed approach can reproduce finger-like structures and super-adiabatic flame temperatures. While these features are highly unstable, they can influence the stationary flame structure. The statistically averaged behaviour of the jet is addressed in the next subsection.

5.2. Mean fields

The temporally and spanwise-averaged fields (denoted by $\langle \cdot \rangle_{t,z}$) provide a more rigorous metric for assessing the ability of the model to predict the macroscopic flame topology. Averaging in z is particularly useful, since it reduces the simulation time required to achieve statistically meaningful results. Furthermore, these mean representations allow for a systematic quantification of the primary modelling variables, specifically the sensitivity to mesh resolution and the physical impacts of Soret and heat loss. In this context, the focus shifts from individual wrinkling events to the spatial distribution of the reaction zone and the long-term stability of the lateral enriched branches.

To aid comparison, the contour corresponding to the scaled, filtered, and time- and spanwise-averaged temperature level $\langle T_s \rangle_{t,z} = 0.6$ is superimposed on the plots, where:

$$\langle T_s \rangle_{t,z} = \frac{\langle \tilde{T} \rangle_{t,z} - T_u}{T_b^{1D} - T_u}. \quad (17)$$

Using this quantity, the distance from the exit of the injector to the point where the iso-line $\langle T_s \rangle_{t,z} = 0.6$ cuts the axis allows the definition of a flame length h_T .

To establish a baseline for the high-resolution predictive capabilities, a side-by-side comparison of the DNS and LES M4 cases, focusing on the averaged controlling variables, $\langle \tilde{Z} \rangle_{t,z}$ and $\langle \tilde{Y}_{H_2O} \rangle_{t,z}$, and the hydrogen source term, $\langle \tilde{\omega}_{H_2} \rangle_{t,z}$ is shown in Fig. 3. This assessment is further extended in Fig. 4, which compares the averaged temperature fields, $\langle \tilde{T} \rangle_{t,z}$, across all mesh resolutions and modelling configurations.

The LES results presented in Fig. 3 qualitatively reproduce the spatial flame structure observed in the DNS, including the two lateral branches. In these regions, both the progress variable and the temperature (see also Fig. 4) increase due to local enrichment of the mixture fraction induced by thermodiffusive effects. The LES slightly overestimates both the spreading angle of the lateral branches and the peak value of the mixture fraction

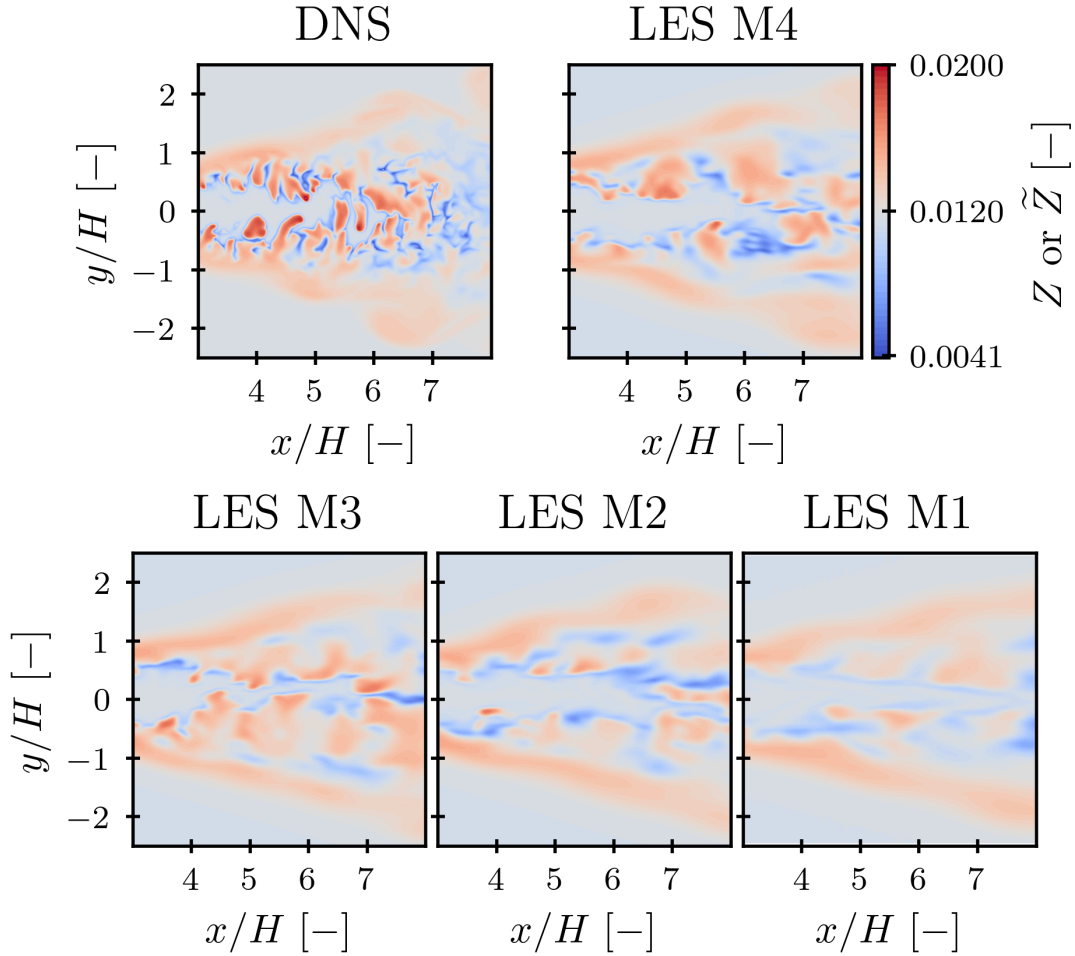


Fig. 2: Instantaneous snapshots of the Z for the DNS and \bar{Z} for LES for each mesh resolution.

and, consequently, those of temperature and progress variable, particularly near the wall edges. In addition, the LES predicts a slightly longer lateral branch than the DNS, although the difference remains small.

Downstream of the flame along the axis, the DNS exhibits a local reduction in the mixture fraction, resulting in sub-adiabatic temperatures. This decrease in mixture fraction is attributed to the conservation of the mixture fraction mass flow rate. The LES qualitatively captures this behaviour, although the effect is slightly underestimated.

Furthermore, the source term distribution indicates that the tabulated combustion model accurately reproduces the turbulent burning velocity, resulting in a flame length and shape that are in close agreement with the DNS. Minor differences are observed in the form of a slightly longer flame and sharper contours near the flame tip. These deviations could partly be attributed to the absence of a physical mechanism to account for sub-filter curvature effects in combination with all the introduced modelling decisions (variance equations, PDF integrations, numerical discretisation, eddy viscosity, among others). Overall, this represents a key outcome of the present study, demonstrating that the essential flame characteristics are captured despite the lack of explicit sub-grid curvature

modelling in the proposed combustion framework.

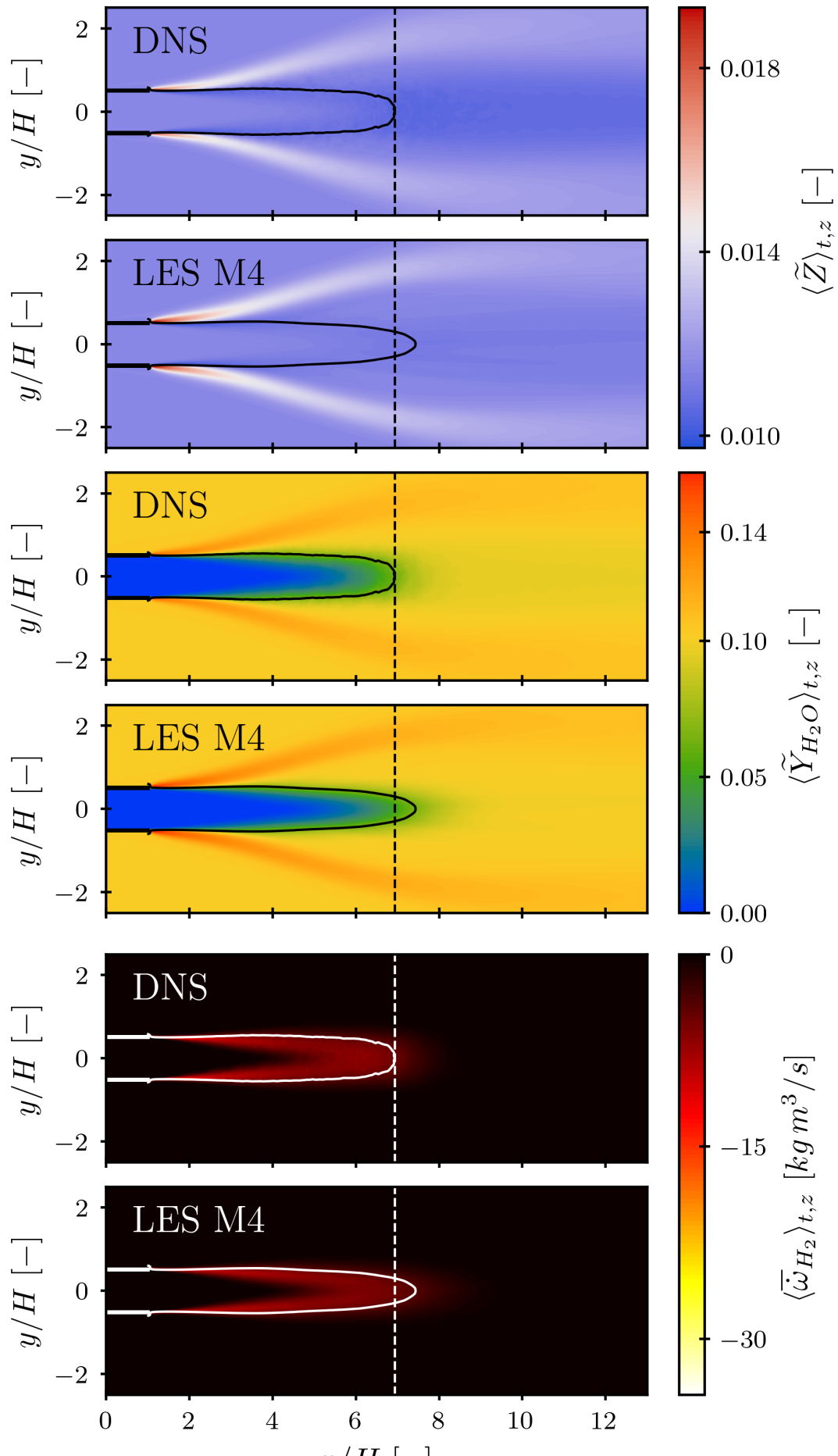
Once the baseline flame topology has been established, it is necessary to separate the respective contributions of numerical resolution and physical modelling choices to the observed macroscopic behaviour. To this end, Fig. 4 presents a dedicated analysis of the averaged temperature field $\langle \widetilde{T} \rangle_{t,z}$, examining four mesh resolutions (M1–M4) as well as configurations in which individual physical modelling components are selectively disabled (M4 without D_k^T and M4 without T_{wall}).

The LES results show that all mesh resolutions (M1–M4) qualitatively reproduce the spatial flame structure observed in the DNS, including the two lateral branches where temperature increases as a result of local mixture fraction enrichment induced by thermodiffusive effects. In addition, the temperature field shows (qualitatively) little sensitivity to resolution, whereas the predicted flame height systematically improves and approaches the DNS value as mesh resolution increases. This is consistent with the improvement in capturing the source term (and consequently the consumption speed) when the resolution increases. This aspect is further clarified by the upcoming analysis of the influence of mesh resolution and thermodiffusion in the distribution of hydrogen's source term in the domain. Finally, as the mesh resolution increases and a larger fraction of the turbulence–chemistry interaction is resolved, the flame tip evolves from a sharper to a more rounded shape, with the higher-resolution LES cases yielding flame geometries that are more consistent with those observed in the DNS.

Concerning the physical modelling, suppressing the Soret effect (M4 without D_k^T) results in a longer flame and lower temperatures in the lateral branches. This behaviour is consistent with the dual role of thermal diffusion in lean hydrogen flames. While the Soret effect typically decreases the one-dimensional laminar flame speed by approximately 5–10%, it simultaneously enhances the diffusivity of light species. In lean hydrogen flames, this preferential transport amplifies thermodiffusive instabilities, thereby increasing the global consumption speed. As a result, simulations that account for the Soret effect exhibit shorter flames than those in which it is neglected [7, 46]. The lower temperatures observed in the lateral branches when thermal diffusion is omitted arise from the absence of preferential migration of light species, particularly H and H₂, towards regions of high curvature or elevated temperature. This suppresses local mixture enrichment within the lateral cells, leading to lower temperatures and less reactive branch structures [7, 46]. Overall, these results highlight the importance of accounting for the Soret effect in hydrogen flame modelling and demonstrate that the present TC approach successfully captures its dominant physical mechanisms.

When heat loss to the burner walls is introduced, a new coordinate is included in the manifold and new terms are added into the governing equations for Z , Y_c and h . Including these effects produces a slight improvement of the mixture fraction reduction observed downstream of the flame. Consequently, this region yields downstream temperatures closer to those of the co-flow. It should be noted, however, that the temperature difference remains limited to approximately 30 K (this point is visualised in more detail in Fig. 6). The magnitude of this discrepancy remains relatively small, suggesting that the addition of the enthalpy coordinate in the manifold, primarily associated with wall heat losses, shows a limited impact on the LES solution.

To move beyond qualitative comparisons and assess the thermochemical state of the mixture, the statistical distributions of the relevant scalars are examined. Figure 5 shows the joint probability density functions (jPDFs)



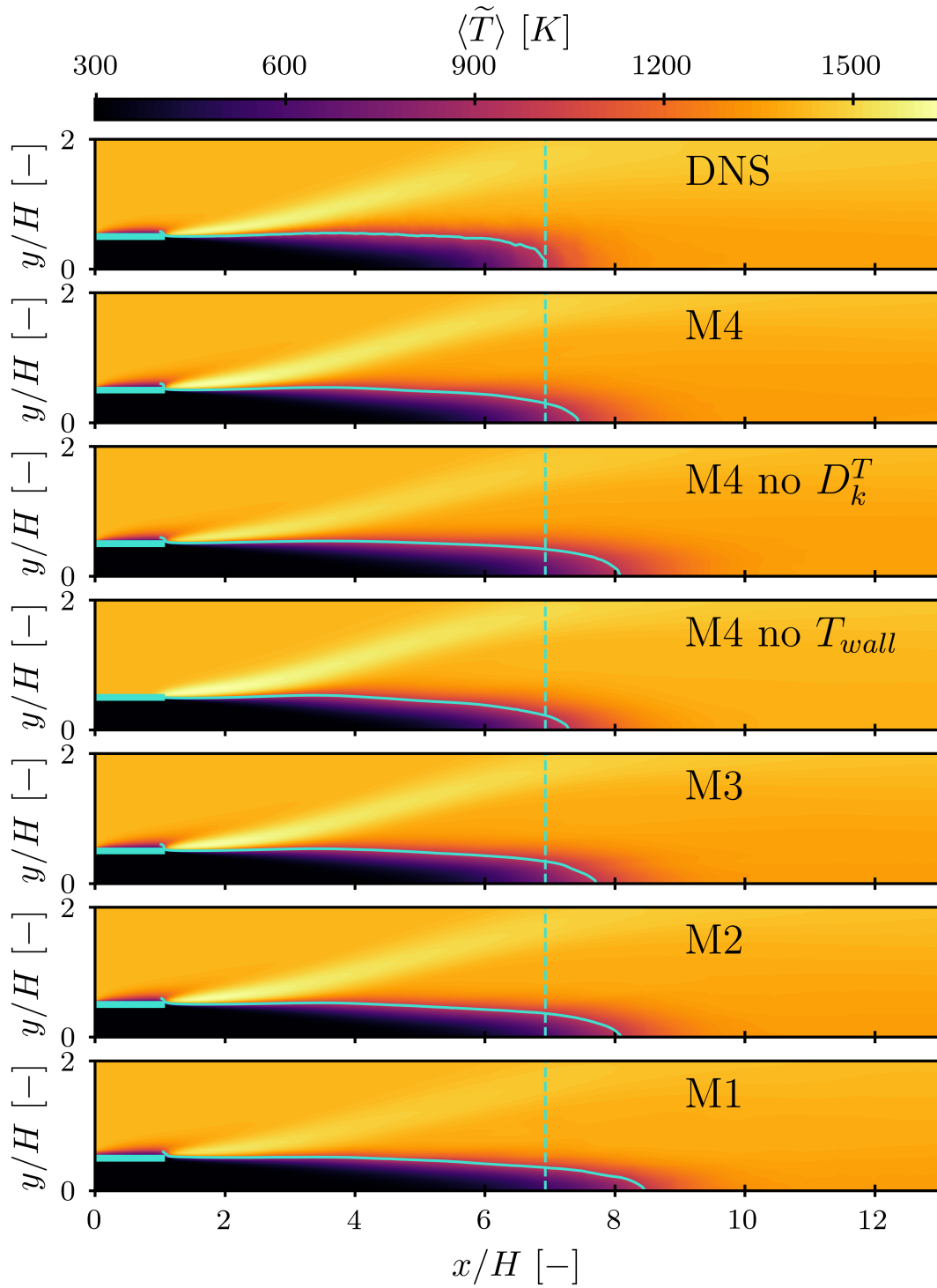


Fig. 4: $\langle \tilde{T} \rangle_{t,z}$ field for the DNS (first panel), the LES with different resolutions and all physics (second to fifth panels), the LES without Soret effect (sixth panel) and the LES without heat losses (seventh panel). Isocontours of $sT = 0.6$ from Eq.(16) (cyan lines) and the DNS flame length h_T are included for reference.

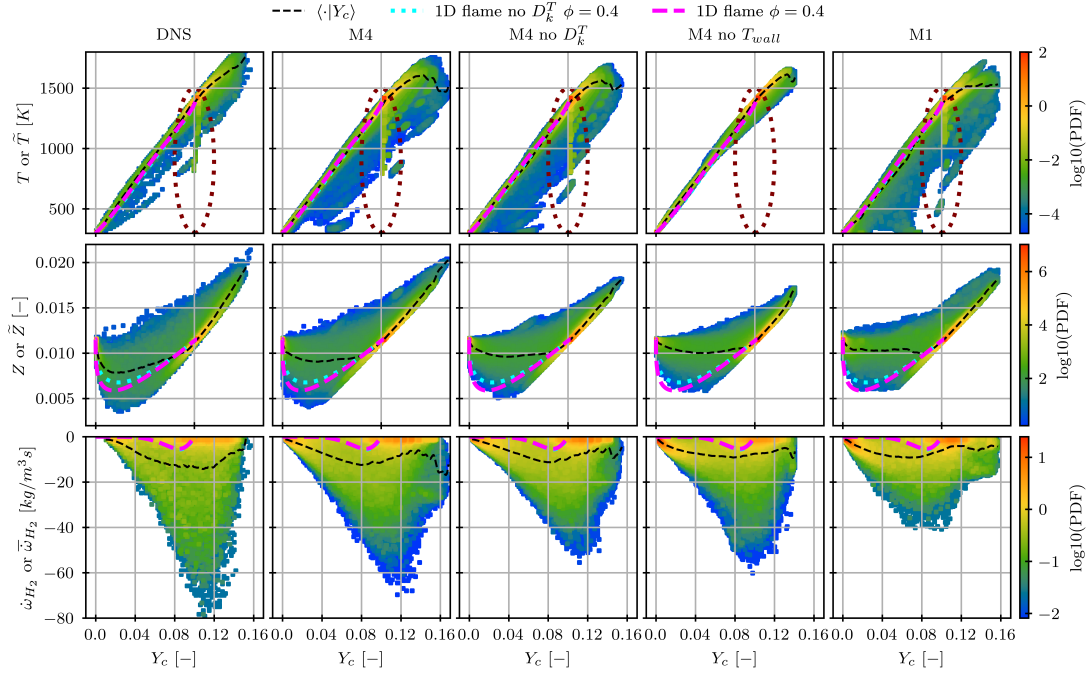


Fig. 5: jPDF of temperature (first row), hydrogen source term (second row) and mixture fraction (third row) with respect to the progress variable for the DNS (first column), LES with resolutions M4 and M1 (columns two and three), LES without Soret effect (column four) and LES without wall heat losses (column five). A maroon ellipse is added to the first row to aid visualisation and highlight the region affected by heat losses.

for the DNS, and the LES for case M4, including those without D_k^T , and without T_{wall} . This comparison enables an evaluation of whether the LES solutions follow the appropriate thermochemical manifold under the various modelling assumptions. Each row shows the jPDF of temperature, mixture fraction, and hydrogen source term as a function of the progress variable. While for the DNS instantaneous values are used, for the LES, these fields are represented using their resolved counterparts. We have checked that filtering the DNS data for the comparison does not qualitatively alter the jPDF (not shown), and since it should be done for different filter sizes, we opt for just using the DNS value. The same representation for the four mesh resolutions, including all physics, is available in the supplementary material.

For the temperature field, the scatter points follow the unstretched one-dimensional flame up to a progress variable of approximately 0.1, corresponding to the equilibrium value of the one-dimensional flame. Beyond this point, super-adiabatic temperatures arise from mixture fraction enrichment driven by curvature effects and interactions with the hot co-flow (lateral branches). As highlighted by the maroon ellipse in the figure, the simulations with wall heat losses exhibit an additional secondary branch of decreasing temperatures near the same progress-variable value, an effect absent in the adiabatic LES (column four). It is highlighted that when either coarsening the mesh or disabling the Soret effect, the jPDF extends over a wider region. However, in all cases, including the adiabatic configuration, where flame spreading is reduced, the conditionally averaged temperature overlaps with the unstretched flame temperature over the range in which the latter is defined.

Both the hydrogen source term and the mixture fraction show clear improvements with increasing mesh resolution (cf. M1 versus M4), with the finer mesh leading to increased hydrogen consumption and the recovery of additional curvature-related features. Owing to thermodiffusive effects at the flame front, the mixture fraction shows noticeable scatter away from the one-dimensional flame manifold. However, the conditional mean remains close to the one-dimensional reference for both the DNS and the highest-resolution LES M4 case. A reduction in the spread of the mixture-fraction distribution is observed when either the Soret effect is disabled or the enthalpy coordinate is suppressed, indicating a diminished influence of thermodiffusive transport under these conditions.

Among the three quantities, the hydrogen source term is the most sensitive. It shows substantial improvement with mesh refinement, while the removal of either physical effect (Soret or enthalpy coordinate with heat loss) leads to a reduction in its magnitude relative to both the DNS and to LES M4. The conditional average of the source term differs significantly from that of the one-dimensional flame due to the strong sensitivity of the reaction rate to the combined effects of mixture fraction and progress variable.

Finally, to establish a more quantitative analysis, the axial and transverse profiles of key flow and scalar quantities are shown in Fig. 6. The analysis focuses on the temporally and spanwise-averaged streamwise velocity $\langle \bar{u}_x \rangle_{t,z}$, mixture fraction $\langle \bar{Z} \rangle_{t,z}$, temperature $\langle \bar{T} \rangle_{t,z}$, and hydrogen reaction rate $\langle \bar{\omega}_{H_2} \rangle_{t,z}$, evaluated along the centreline ($y/H = 0$) and at two downstream transverse locations ($x/H = 4$ and 6).

Overall, the finest-resolution case (LES M4) exhibits the closest agreement with the DNS across all examined quantities. The streamwise velocity profiles are well reproduced by all simulations, with the LES capturing the characteristic multi-peak structure. Near the flame base, the DNS shows an initial decrease in velocity up to approximately $x/H = 5$, associated with jet spreading. This behaviour is consistently recovered by all LES cases. Further downstream, the subsequent increase in velocity is linked to the local rise in temperature resulting from intense heat release, which modifies the density field and, through mass conservation, accelerates the flow. Consistent with the preceding velocity decrease, the LES predictions accurately capture the axial locations of the temperature and heat-release peaks. Both simulations predict the maximum velocity, and hence, the flame length at nearly the same axial position. The jet flame exhibits a progressive redistribution of momentum from the jet core to the surrounding flow, resulting in a gradual decrease in axial velocity and a corresponding reduction in heat release. In the transverse direction, the velocity profiles decay smoothly until reaching the region affected by the lateral temperature branches induced by the co-flow interaction, beyond which the velocity asymptotically approaches the co-flow value.

Moreover, all simulations reproduce the sharp increase in temperature across the reaction zone, as evidenced by the axial profiles. It is noted, however, that the LES M4 case without the enthalpy coordinate exhibits a higher peak temperature, consistent with the earlier analysis of the mean temperature fields, with values approaching the adiabatic one-dimensional flame temperature ($T_b^{1D} = 1421.95$ K, indicated on the temperature axis for reference), although the quantitative differences remain small from a practical standpoint. With respect to the mixture-fraction profile, the DNS shows a pronounced axial reduction associated with mixture-fraction conservation. This behaviour is partially captured by LES M4, although it underpredicts the final value as pointed out in the previous section. In contrast, disabling either the Soret effect or the heat loss reduces the mixture fraction variation across

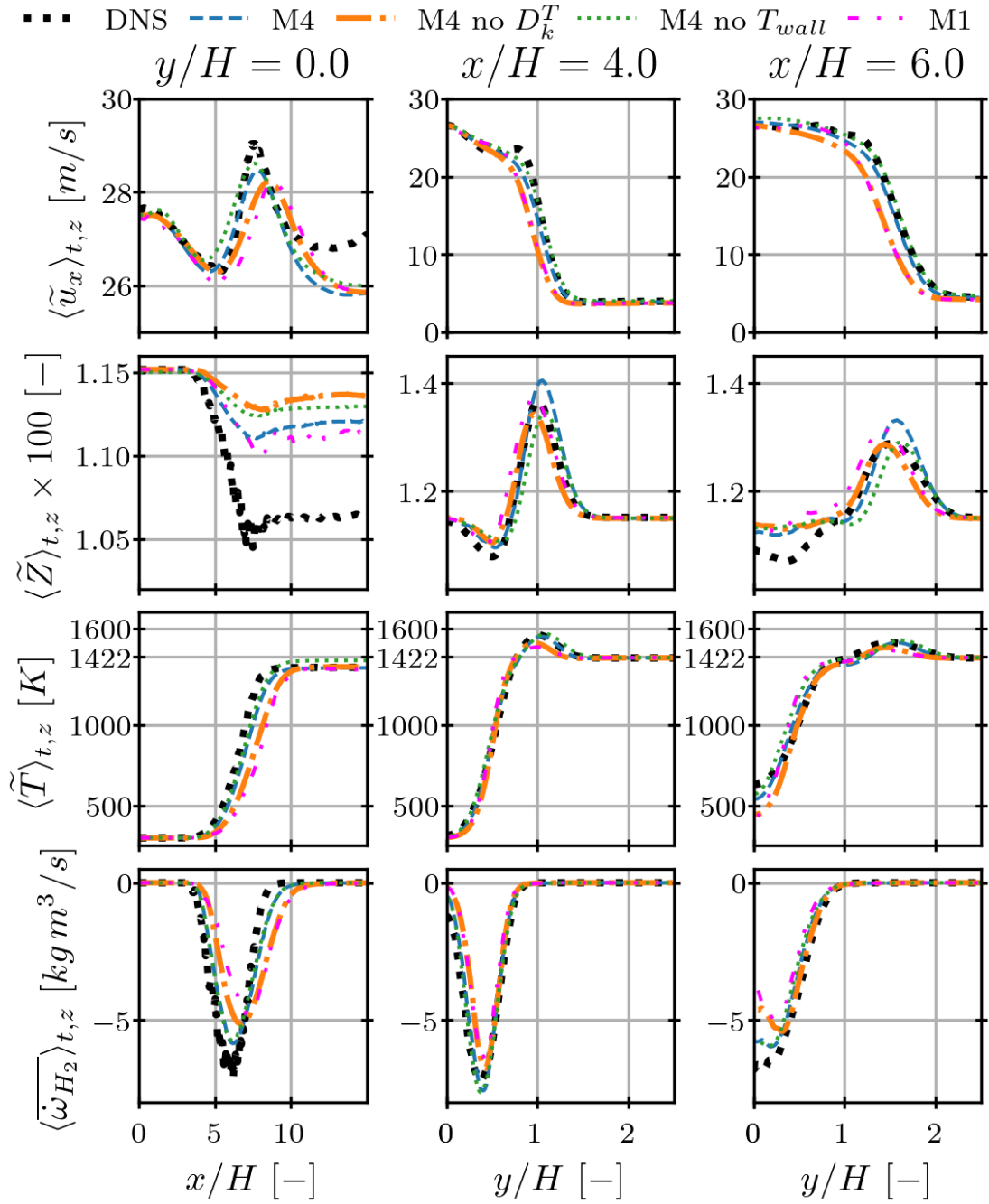


Fig. 6: Temporally and spatially averaged plots of $\langle \tilde{u}_x \rangle_{t,z}$ (row 1), $\langle \tilde{Z} \rangle_{t,z}$ (row 2), $\langle \tilde{T} \rangle_{t,z}$ (row 3) and $\langle \tilde{\omega}_{H_2} \rangle_{t,z}$ (row 4) profiles along $y/H = 0$ (column 1), $x/H = 4$ (column 2) and $x/H = 6$ (column 3) for the DNS (dotted black lines), LES M4 (dashed blue lines), LES M4 no D_k^T (dash-dot orange lines), LES M4 no T_{wall} (dotted green lines) and LES M1 (dash-dot-dot pink lines).

the flame front. Changes in the mixture fraction within the lateral branches are also consistently captured across all cases. These reductions in mixture fraction correspond to the observed variations in the hydrogen reaction rate, of which all simulations reproduce the location and shape of the reaction-rate peak with good accuracy. Overall, the LES results are in good agreement with the DNS, with the largest deviations found in LES M1, highlighting the influence of mesh resolution. The comparisons emphasise that mesh resolution, thermal diffusion, and enthalpy effects each play a specific role in accurately reproducing the DNS flame structure and reaction-rate dynamics. The same figure, including all mesh resolutions, is provided in the supplementary material.

5.3. Macroscopic parameters of the flame

Whereas the previous sections assessed the accuracy of local thermodynamic properties, the present section characterises the global flame behaviour using statistically averaged quantities, with a focus on the model's ability to predict integrated metrics that are directly relevant to practical applications.

We first evaluate the fuel flux as a function of height ($\mathcal{F}(x)$), defined as the temporal and spanwise average of the H_2 mass flux, followed by the integration over the remaining spatial directions:

$$\mathcal{F}(x) = \frac{1}{\rho_u U H Y_{H_2,u}} \int \overline{\langle \rho u_x Y_{H_2} \rangle_{t,z}}(x, y) dy, \quad (18)$$

where ρ_u is the unburnt gas density, U is the bulk inlet velocity of the jet, H is the slot width, and $Y_{H_2,u}$ is the hydrogen mass fraction in the unburnt gases.

The axial evolution of fuel flux is shown in Fig. 7 for the DNS and all LES modelling strategies, providing a clear illustration of the influence of transport modelling and mesh resolution on the global flame length. The plot shows a good correlation between the DNS and LES M4 results. Adding the heat loss through a new manifold coordinate for the enthalpy leads to a modest reduction in the fuel-consumption rate, though this effect may be considered small in this case. In contrast, suppressing the Soret effect has a greater impact, as the associated reduction in local burning rates results in a substantial increase in the predicted flame height. These results confirm that, for lean hydrogen mixtures, neglecting thermal diffusion systematically overpredicts the flame length.

In addition, the flame height, consumption speed, and flame topology, quantified through the flame surface perimeter, are examined. The flame height is first evaluated using the previously defined metric h_T , corresponding to the maximum x -coordinate of a closed temperature isoline obtained from Eq. (17) at $\langle sT \rangle = 0.6$. Furthermore, the definition of the fuel consumption given in Eq. (18) enables the introduction of an alternative flame-height measure, $h_{\mathcal{F}}$, defined by a threshold criterion at $\mathcal{F} = 0.05$ [24].

The consumption speed, $\overline{s_c}$, defined as the averaged hydrogen-consumption rate, and the flame perimeter (instead of surface due to the averages in z), $l(\langle sT \rangle)$, where $\langle sT \rangle$ denotes the isoline of the averaged scaled temperature defined in Eq. (17), are evaluated along the corresponding mean temperature isoline as follows:

$$l(\langle sT \rangle) = \text{length of isoline at value } (\langle sT \rangle). \quad (19)$$

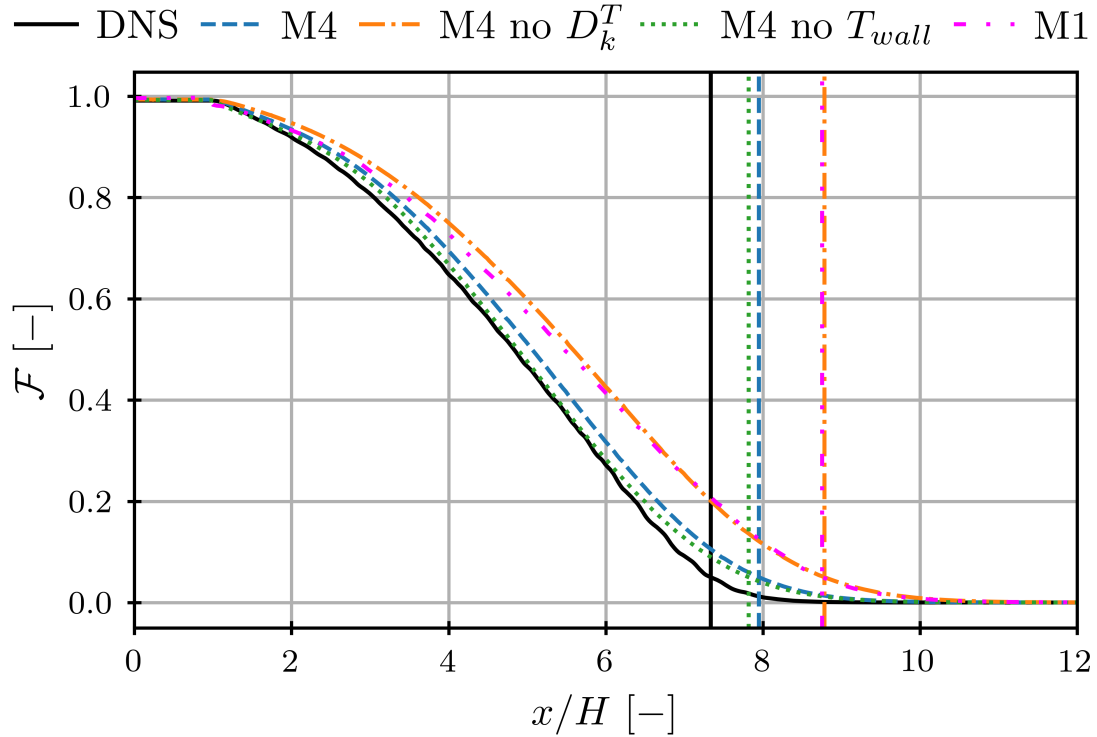


Fig. 7: Fuel consumption for the DNS and the LES study cases. The flame height h_f is included with vertical lines for the different cases.

Case	h_f/H	h_f/H	l/H	\bar{s}_c/s_L^0
DNS	7.34	6.93	12.39	11.27
LES M4	7.95	7.43	13.20	9.88
LES M4 no D_k^T	8.78	8.07	14.46	8.67
LES M4 no T_{wall}	7.82	7.28	12.75	10.04
LES M3	8.10	7.71	13.69	8.84
LES M2	8.46	8.10	14.38	8.71
LES M1	8.75	8.45	15.02	7.76

Table 2: LES macro-parameters. Results for the consumption speed are scaled with the unstretched laminar flame speed s_L^0 at $\phi = 0.4$ with constant Lewis numbers for the DNS and mixture-averaged transport for the LES.

$$\bar{s}_c(\langle sT \rangle) = -\frac{1}{\rho_u Y_{H_2,u} l(\langle sT \rangle)} \int_A \langle \bar{\omega}_{H_2} \rangle_{t,z} dS, \quad (20)$$

Table 2 summarises the results for the different flame height definitions, consumption speed, and flame surface perimeter for the DNS and all LES cases.

The flame height is generally comparable across all simulations. Increasing the mesh resolution leads to clear convergence towards the DNS, although this quantity is not particularly sensitive to resolution, and even coarser meshes provide reasonably accurate predictions. The LES effectively captures both consumption speed and flame-

surface perimeter, with relative errors on the finest mesh restricted to 12.33% and 6.54%, respectively. For the flame height measures, the errors are also in the same ranges, with 8.31% for $h_{\mathcal{F}}$, and 7.22% for h_T . Consistent with previous observations, neglecting the Soret effect leads to a reduction in the consumption speed with a corresponding increase in the flame length, highlighting the importance of thermal diffusion even for turbulent flames simulated with LES where sub-filter effects play an important role. In contrast, the influence of heat loss remains modest in this configuration since the interaction with the walls is minor. Overall, these findings demonstrate the robustness and reliability of the proposed tabulated flamelet model for predicting key flame characteristics using a simple turbulent chemistry interaction model based on presumed-shape PDF with beta functions in mixture fraction and progress variable. The results indicate that this modelling approach is sufficient for the present conditions, while more complex closures may be required to fully account for unresolved sub-filter effects on more complex scenarios.

6. Conclusions and future work

In this study, a tabulated flamelet model accounting for differential and preferential diffusion is applied to large-eddy simulations of a planar turbulent premixed jet flame over a range of mesh resolutions and different physical features. The results are compared with those from the reference DNS of Berger et al. [24] showing that the model accurately reproduces the global flame structure and its main characteristics, while providing insights into the role of unresolved sub-filter effects on local thermochemical behaviour.

The turbulent burning velocity and corresponding flame height are well predicted, as confirmed by the mean temperature fields. The interaction between the jet and the co-flow is also captured, including the formation of laterally enriched mixture fraction branches driven by differential diffusion, which lead to locally super-adiabatic temperatures. While the location of these branches is accurately reproduced, a slight overprediction of the mixture enrichment is also observed.

Limitations related to sub-filter curvature effects are identified but remain minor for the conditions considered. With increasing mesh resolution, a larger fraction of the turbulence–chemistry interaction is resolved, resulting in smoother flame-tip geometries and improved agreement with the rounded flame shape observed in the DNS. Quantitative comparisons of axial and transverse profiles show good overall agreement, with discrepancies decreasing systematically with mesh refinement. An assessment of global flame behaviour based on statistically averaged and integrated metrics shows good agreement with the DNS. The analysis confirms that the model accurately predicts flame height, consumption speed, and flame morphology, with limited sensitivity to mesh resolution and heat loss under the present conditions.

The analysis of thermal diffusion highlights the role of the Soret effect when modelling hydrogen flames, which enhances mixture reactivity, increases the consumption speed, and shortens the flame, whereas its omission leads to significant deviations in the predicted behaviour. Incorporating heat loss effects through an additional manifold coordinate provides only marginal improvement since no significant heat-loss effects are present in this problem, and thus the adiabatic formulation remains sufficiently accurate for this case.

Overall, despite unresolved sub-filter effects, the proposed turbulent combustion model captures the primary flame structure and its dominant characteristics, supporting its extension to more advanced sub-filter turbulent-

chemistry interaction models and its application to more practical applications of industrial interest.

CrediT authorship contribution statement

Emiliano Manuel Fortes: Formal analysis, Investigation, Data curation, Software, Visualisation, Writing – original draft. **Eduardo Javier Pérez-Sánchez:** Supervision, Formal analysis, Investigation, Software, Visualisation, Writing – original draft. **Temistocle Grenga:** Supervision, Methodology, Formal analysis, Writing – original draft. **Michael Gauding:** Formal analysis, Resources, Writing – original draft. **Heinz Pitsch:** Formal analysis, Resources, Writing – original draft. **Daniel Mira:** Supervision, Methodology, Formal analysis, Funding acquisition, Project administration, Resources, Writing – original draft.

Declaration of competing interest

The authors declare that they have no known competing financial interests or personal relationships that could have appeared to influence the work reported in this paper.

Acknowledgments

The research leading to these results has received funding from the European Union's Horizon 2020 Programme under the Horizon Europe HyInHeat project GA 101091456 and H2AERO CPP2022-009921 both funded by MICIU/AEI/10.13039/501100011033 and by "European Union NextGenerationEU/PRTR". EMF acknowledges the predoctoral grant Joan Oró-FI (2023 FI-1 00680) funded by AGAUR from the Secretariat of Universities and Research of the Department of Research and Universities of the Generalitat de Catalunya and the ESF+. DM acknowledges the Grant RYC2021-034654 funded by MICIU/AEI/10.13039/501100011033 and by "European Union NextGenerationEU/PRTR". EJPS acknowledges his AI4S fellowship within the "Generación D" initiative by Red.es, Ministerio para la Transformación Digital y de la Función Pública, for talent attraction (C005/24-ED CV1), funded by NextGenerationEU through PRTR. The authors also acknowledge computational resources by the EuroHPC allocation EHPC-REG-2023R03-194 and RES allocation IM-2025-2-0035 provided by BSC.

Supplementary material

Supplementary material is submitted along with the manuscript. This supplementary material provides technical details supporting the modelling choices and the mesh sensitivity analysis presented in the main text. First, a visualisation of each mesh resolution is provided. Second, the thermochemical properties of the 1D flames are analysed to justify the transition from the constant-Lewis-number approach used in the DNS to the mixture-averaged transport model employed in the Large-Eddy Simulations (LES) manifold. Third, an extended sensitivity analysis is provided, including joint Probability Density Functions (jPDFs) and axial profiles for all mesh resolutions, further quantifying the convergence of the LES toward the reference DNS data.

Mesh resolutions

Figure 8 illustrates the mesh resolution in the directions of the x and y axes with respect to the dns spacing $\delta_{x,z}^{\text{DNS}} = 70 \mu\text{m}$. The perimeter of scaled temperature defined in the main text for the simulation LES M4 is included for reference on the mesh resolution according and flame height. In the z axes, the spacing is $dz/\delta_{x,z}^{\text{DNS}} = 6, 3, 2$ and 1.5 for M1, M2, M3 and M4, respectively.

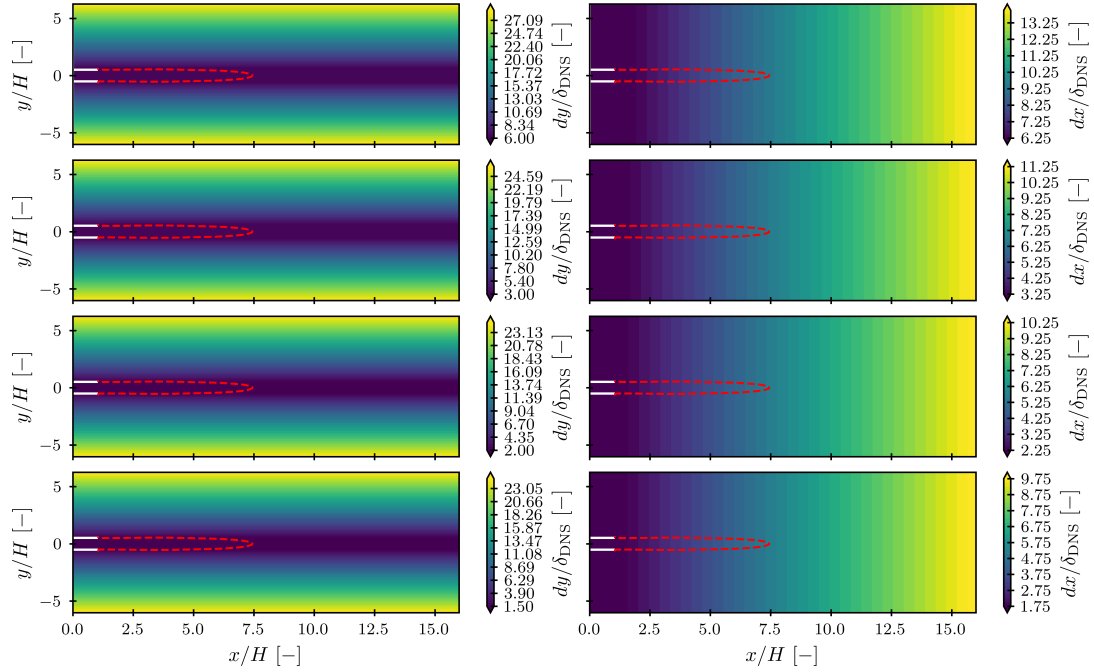


Fig. 8: Contour plots of $dy/\delta_{x,z}^{DNS}$ (first column) and dx/δ_{DNS} (second column) for each mesh resolution M1 (first row), M2 (second row), M3 (third row) and M4 (fourth row). Dashed red lines indicate the flame perimeter for LES M4.

6.1. One-dimensional flames and transport validation

Table 3 summarises the primary thermochemical properties of the one-dimensional (1D) flames at the jet injection conditions ($\phi = 0.4$). To validate the consistency of the modelling framework, calculations were performed using three approaches: the mixture-averaged transport approximation (both with and without the Soret effect) and the constant Lewis number (Le) formulation adjusted according to the methodology of Berger et al. [24]. All 1D calculations were performed using the open-source software Cantera [37].

The results demonstrate that the global flame macroparameters of laminar burning velocity (s_L) and thermal flame thickness (l_F) exhibit negligible deviations between the adjusted constant Le and mixture-averaged models. This alignment provides a critical justification for benchmarking the current LES results against the DNS data. It ensures that any observed differences in the three-dimensional turbulent flame structure are attributable to sub-filter modelling and turbulence-chemistry interaction rather than fundamental discrepancies in the underlying laminar flame structure. Furthermore, comparing the mixture-averaged results with and without thermal diffusion shows that the Soret effect significantly influences the local consumption rate, necessitating its inclusion for an accurate representation of lean hydrogen flame chemistry.

To reinforce this validation, it is essential to verify the model agreement not only at the nominal injection equivalence ratio but across the entire range of ϕ values encountered in the turbulent jet. Fig. 9 illustrates the laminar burning velocity (s_L) and thermal flame thickness (l_F) as a function of the equivalence ratio (ϕ). The results demonstrate negligible deviations between the adjusted constant Lewis number approach and the mixture-averaged

Label	D_k^T	s_L [cm/s]	l_F [μm]	τ [ms]
Mix-avg	On	18.3	681.3	3.72
Mix-avg no D_k^T	Off	19.2	665.8	3.47
Le cst	On	18.0	698.7	3.91

Table 3: Flame properties of the main injection mixture at $\phi = 0.4$, $T = 298\text{K}$ and $p = 1$ atm using mixture-averaged transport with and without thermal diffusion, and using constant Lewis numbers with thermal diffusion.

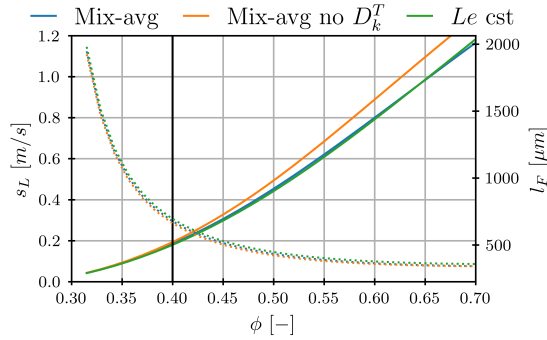


Fig. 9: Comparison of laminar burning velocity s_L (left y axis) and thermal flame thickness l_F (right y axis) as a function of the equivalence ratio ϕ for hydrogen–air mixtures at $T_u = 298$ K and $p = 1$ atm. Solid lines denote s_L for the mixture-averaged transport model with the Soret effect (blue lines), mixture-averaged transport without the Soret effect (orange lines), and the adjusted constant Lewis number formulation (green lines). The same colour code is used for the dotted lines in l_F .

transport model across the equivalence ratios relevant to this study. This agreement ensures a consistent and fair comparison between the DNS and LES frameworks. Additionally, results for the mixture-averaged transport model without thermal diffusion ($D_k^T = 0$) are included to highlight the magnitude of Soret effects on the flame properties.

6.2. Extended mesh sensitivity analysis

This section provides a comprehensive evaluation of the sensitivity of the LES results to mesh resolution, ranging from the coarsest (M1) to the finest (M4) grids. The results are systematically compared against the reference DNS data to quantify the convergence of both local thermochemical states and global flame parameters.

Figure 10 illustrates how mesh convergence systematically improves the jPDF distribution of the analysed quantities. As the mesh resolution is increased, the mixture fraction field captures a broader scatter range, reflecting the increased resolution of local enrichment and depletion zones. A similar trend is observed for the source term, which remains the most grid-sensitive quantity, as finer meshes more accurately resolve high-reactivity peaks that are typically smoothed out on coarser grids.

The impact of resolution on the mean flame structure is further quantified through axial and transverse profiles of velocity, temperature, mixture fraction, and hydrogen source term. While global features, such as the velocity decay, are captured even on coarser grids, the accurate prediction of the peak reaction rate, peak velocities, and the specific axial location of the flame tip requires finer resolution as shown by the comparative results from mesh M1 to M4. In contrast, the decay of the mixture fraction is less sensitive to mesh resolution, which suggests that further improvements would require more advanced sub-filter modelling.

Finally, the influence of mesh resolution on fuel consumption is clearly evident, with the integrated consumption

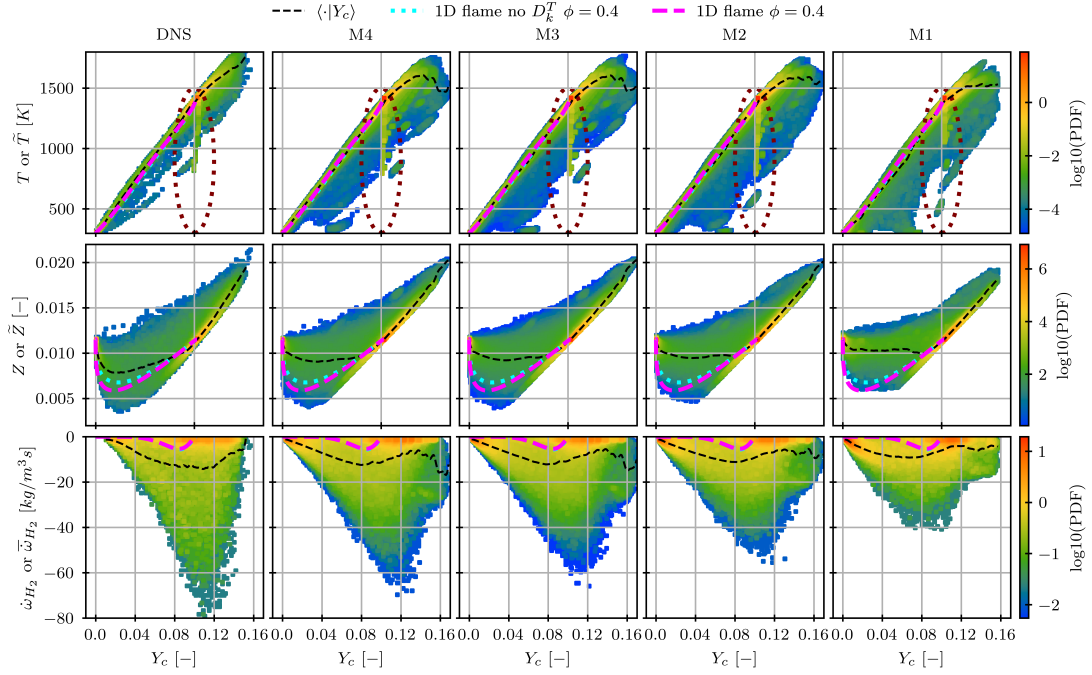


Fig. 10: jPDF of temperature (first row), hydrogen source term (second row) and mixture fraction (third row) with respect to the reactive progress variable for the DNS (first column), and the LES with resolutions M4, M1, M2 and M3 (columns two to five).

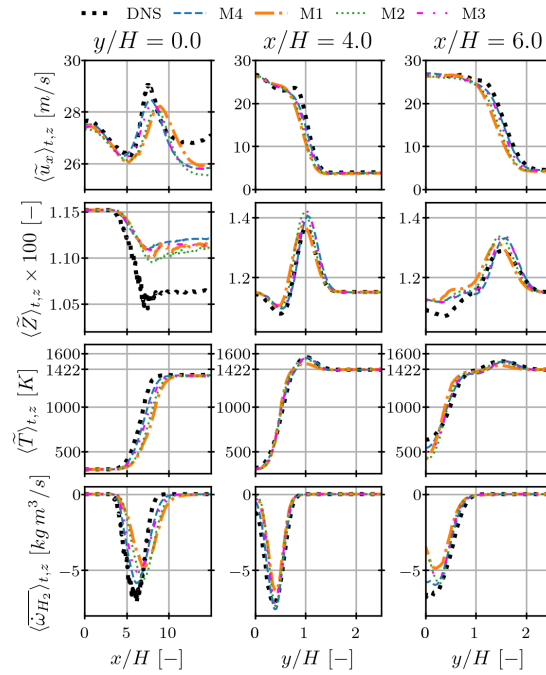


Fig. 11: Temporally and spatially averaged plots of $\langle \tilde{u}_x \rangle_{t,z}$ (row 1), $\langle \tilde{Z} \rangle_{t,z}$ (row 2), $\langle \tilde{T} \rangle_{t,z}$ (row 3) and $\langle \tilde{\omega}_{H_2} \rangle_{t,z}$ (row 4) profiles along $y/H = 0$ (column 1), $x/H = 4$ (column 2) and $x/H = 6$ (column 3) for the DNS (dotted black lines), LES M4 (dashed blue lines), LES M3 (dash-dot orange lines), LES M2 (dotted green lines) and LES M1 (dash-dot-dot pink lines).

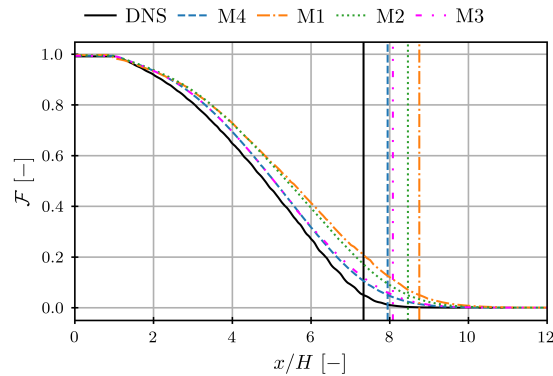


Fig. 12: Fuel consumption for the DNS and the LES with all mesh resolutions. Flame height h_F is included with vertical lines.

rate converging towards the DNS reference as the grid is refined. The small differences observed between the M3 and M4 cases indicate that statistical convergence and almost mesh independence for this global metric are effectively achieved at the higher resolutions.

References

- [1] H. Pitsch, The transition to sustainable combustion: Hydrogen- and carbon-based future fuels and methods for dealing with their challenges, *Proceedings of the Combustion Institute* 40 (1) (2024) 105638.
- [2] L. Berger, A. Attili, M. Gauding, H. Pitsch, LES combustion model for premixed turbulent hydrogen flames with thermodiffusive instabilities: a priori and a posteriori analysis, *Journal of Fluid Mechanics* 1003 (2025) A33.
- [3] L. Berger, A. Attili, H. Pitsch, Intrinsic instabilities in premixed hydrogen flames: Parametric variation of pressure, equivalence ratio, and temperature. part 1: dispersion relations in the linear regime, *Combust. Flame* 240 (2022) 111935.
- [4] E. M. Fortes, E. J. Pérez-Sánchez, A. Both, T. Grenga, D. Mira, Analysis of thermodiffusive instabilities in hydrogen/air premixed flames using a tabulated flamelet model, *International Journal of Hydrogen Energy* 137 (2025) 247–259.
- [5] M. Matalon, The Darrieus–Landau instability of premixed flames, *Fluid Dynamics Research* 50 (5) (2018) 051412.
- [6] J. F. Grcar, J. B. Bell, M. S. Day, The soot effect in naturally propagating, premixed, lean, hydrogen–air flames, *Proceedings of the Combustion Institute* 32 (1) (2009) 1173–1180.
- [7] Z. Zhou, F. E. Hernández-Pérez, Y. Shoshin, J. A. van Oijen, L. P. de Goeij, Effect of Soret diffusion on lean hydrogen/air flames at normal and elevated pressure and temperature, *Combustion Theory and Modelling* 21 (5) (2017) 879–896.
- [8] J. Schlup, G. Blanquart, Validation of a mixture-averaged thermal diffusion model for premixed lean hydrogen flames, *Combustion Theory and Modelling* 22 (2) (2017) 264–290.
- [9] D. Mira, E. J. Pérez-Sánchez, R. Borrell, G. Houzeaux, HPC-enabling technologies for high-fidelity combustion simulations, *Proceedings of the Combustion Institute* 39 (4) (2023) 5091–5125.
- [10] A. Vreman, J. Van Oijen, L. De Goeij, R. Bastiaans, Direct numerical simulation of hydrogen addition in turbulent premixed bunsen flames using flamelet-generated manifold reduction, *Int. J. Hydrogen Energ.* 34 (2009) 2778–2788.
- [11] J. de Swart, R. Bastiaans, J. van Oijen, L. de Goeij, R. Cant, Inclusion of preferential diffusion in simulations of premixed combustion of hydrogen/methane mixtures with flamelet generated manifolds, *Flow Turbul. Combust.* 85 (2010) 473–511.
- [12] A. Donini, R. Bastiaans, J. Van Oijen, L. De Goeij, Differential diffusion effects inclusion with flamelet generated manifold for the modeling of stratified premixed cooled flames, *Proc. Combust. Inst.* 35 (2015) 831–837.
- [13] E. Abtahzadeh, P. de Goeij, J. van Oijen, Development of a novel flamelet-based model to include preferential diffusion effects in autoignition of CH₄/H₂ flames, *Combust. Flame* 162 (2015) 4358–4369.
- [14] H. Nicolai, L. Dressler, J. Janicka, C. Hasse, Assessing the importance of differential diffusion in stratified hydrogen–methane flames using extended flamelet tabulation approaches, *Physics of Fluids* 34 (8) (2022) 085118.
- [15] K. Dinesh, X. Jiang, J. Van Oijen, R. Bastiaans, L. De Goeij, Hydrogen-enriched nonpremixed jet flames: effects of preferential diffusion, *Int. J. Hydrogen Energ.* 38 (2013) 4848–4863.
- [16] A. Donini, R. M. Bastiaans, J. Van Oijen, L. H. de Goeij, A 5-D implementation of fgm for the large eddy simulation of a stratified swirled flame with heat loss in a gas turbine combustor, *Flow Turbul. Combust.* 98 (2017) 887–922.
- [17] F. Almutairi, K. R. Dinesh, J. van Oijen, Modelling of hydrogen-blended dual-fuel combustion using flamelet-generated manifold and preferential diffusion effects, *Int. J. Hydrogen Energ.* 48 (2023) 1602–1624.
- [18] J. Regele, E. Knudsen, H. Pitsch, G. Blanquart, A two-equation model for non-unity lewis number differential diffusion in lean premixed laminar flames, *Combust. Flame* 160 (2013) 240–250.
- [19] J. Schlup, G. Blanquart, Reproducing curvature effects due to differential diffusion in tabulated chemistry for premixed flames, *Proc. Combust. Inst.* 37 (2019) 2511–2518.

- [20] H. Böttler, X. Chen, S. Xie, A. Scholtissek, Z. Chen, C. Hasse, Flamelet modeling of forced ignition and flame propagation in hydrogen-air mixtures, *Combust. Flame* 243 (2022) 112125.
- [21] H. Böttler, H. Lulic, M. Steinhausen, X. Wen, C. Hasse, A. Scholtissek, Flamelet modeling of thermo-diffusively unstable hydrogen-air flames, *Proc. Combust. Inst.* 39 (2023) 1567–1576.
- [22] N. Mukundakumar, D. Efimov, N. Beishuizen, J. van Oijen, A new preferential diffusion model applied to fgm simulations of hydrogen flames, *Combust. Theor. Model* 25 (2021) 1245–1267.
- [23] L. Berger, A. Attili, J. Wang, K. Maeda, H. Pitsch, Development of large-eddy simulation combustion models for thermally diffusive instabilities in turbulent hydrogen flames, *Proc. Summer Program, CTR, Stanford University* (2022) 247.
- [24] L. Berger, A. Attili, H. Pitsch, Synergistic interactions of thermally diffusive instabilities and turbulence in lean hydrogen flames, *Combustion and Flame* 244 (2022) 112254.
- [25] G. Ferrante, G. Eitelberg, I. Langella, Differential diffusion modelling for LES of premixed and partially premixed flames with presumed FDF, *Combustion Theory and Modelling* (2024) 1–36.
- [26] A. Masucci, T. Ghisu, A. Giusti, Numerical investigation of premixed and non-premixed hydrogen flames using large-eddy simulations and flamelet models, *Journal of Engineering for Gas Turbines and Power* 147 (12) (Sep. 2025).
- [27] E. Pérez-Sánchez, E. Fortes, D. Mira, Assessment of the flamelet generated manifold method with preferential diffusion modeling for partially premixed hydrogen flames, *Combustion and Flame* 277 (2025) 114141.
- [28] S. Bottari, F. D'Alessio, C. Matteucci, P. Lapenna, F. Creta, Data-driven modeling of the flame composition space of an intrinsically unstable lean premixed ammonia/hydrogen/air flame, *Fuel* 405 (2026) 136805.
- [29] M. Schneider, F. Z. Rong, C. Hasse, H. Nicolai, Combustion modelling for the flame-wall interaction of thermally diffusive unstable hydrogen/air flames, *Journal of Fluid Mechanics* 1029 (2026) A36.
- [30] S. Gövert, D. Mira, J. Kok, M. Vázquez, G. Houzeaux, The effect of partial premixing and heat loss on the reacting flow field prediction of a swirl stabilized gas turbine model combustor, *Flow Turbul. Combust.* 100 (2018) 503–534.
- [31] V. Giovangigli, Convergent iterative methods for multicomponent diffusion, *IMPACT of Computing in Science and Engineering* 3 (3) (1991) 244–276.
- [32] M. Burke, M. Chaos, Y. Ju, F. Dryer, S. Klippenstein, Comprehensive H₂/O₂ kinetic model for high-pressure combustion, *International Journal of Chemical Kinetics* 44 (7) (2012) 444–474.
- [33] A. Vreman, An eddy-viscosity subgrid-scale model for turbulent shear flow: Algebraic theory and applications, *Physics of fluids* 16 (10) (2004) 3670–3681.
- [34] A. Both, O. Lehmkuhl, D. Mira, M. Ortega, Low-dissipation finite element strategy for low mach number reacting flows, *Comput. Fluids* 200 (2020) 104436.
- [35] M. Vázquez, G. Houzeaux, S. Koric, A. Artigues, J. Aguado-Sierra, R. Arís, D. Mira, H. Calmet, F. Cucchietti, H. Owen, A. Taha, E. Burness, J. Cela, M. Valero, Alya: Multiphysics engineering simulation toward exascale, *J. Comput. Sci.* 14 (2016) 15–27.
- [36] E. Castillo, R. Codina, Stabilized stress-velocity-pressure finite element formulations of the Navier-Stokes problem for fluids with non-linear viscosity, *Comput. Method. Appl. M.* 279 (2014) 554–578.
- [37] D. Goodwin, H. Moffat, I. Schoegl, R. Speth, B. Weber, Cantera: An object-oriented software toolkit for chemical kinetics, thermodynamics, and transport processes (2023). doi : 10.5281/zenodo.8137090.
URL <https://www.cantera.org>
- [38] S. Chapman, T. G. Cowling, *The Mathematical theory of non-uniform gases*, 3rd Edition, Cambridge Univ. Pr., Cambridge [u.a.], 1999.
- [39] P. Paul, J. Warnatz, A re-evaluation of the means used to calculate transport properties of reacting flows, *Symposium (International) on Combustion* 27 (1) (1998) 495–504.
- [40] T. Zirwes, A. Kronenburg, Assessment of approximate sorlet diffusion models for hydrogen and ammonia combustion, *Flow, Turbulence and Combustion* (Jul. 2025).
- [41] J. van Oijen, F. Lammers, L. de Goey, Modeling of complex premixed burner systems by using flamelet-generated manifolds, *Combustion and Flame* 127 (3) (2001) 2124–2134.
- [42] G. Joulin, T. Mitani, Linear stability analysis of two-reactant flames, *Combustion and Flame* 40 (1981) 235–246.
- [43] G. I. Sivashinsky, Diffusional-thermal theory of cellular flames, *Combustion Science and Technology* 15 (3–4) (1977) 137–145.
- [44] H. Owen, G. Chrysokentis, M. Avila, D. Mira, G. Houzeaux, R. Borrell, J. C. Cajas, O. Lehmkuhl, Wall-modeled large-eddy simulation in a finite element framework, *International Journal for Numerical Methods in Fluids* 92 (1) (2020) 20–37.
- [45] L. Berger, A. Attili, H. Pitsch, Intrinsic instabilities in premixed hydrogen flames: parametric variation of pressure, equivalence ratio, and temperature. part 2: Non-linear regime and flame speed enhancement, *Combust. Flame* 240 (2022) 111936.
- [46] T. Howarth, M. Day, H. Pitsch, A. Aspden, Thermal diffusion, exhaust gas recirculation and blending effects on lean premixed hydrogen flames, *Proceedings of the Combustion Institute* 40 (1–4) (2024) 105429.